Integration of contractile forces during tissue invagination

Integration of contractile forces during tissue invagination

Adam C. Martin[1], Michael Gelbart[2], Rodrigo Fernandez-Gonzalez[3],

Matthias Kaschube[2], Eric F. Wieschaus[1]

[1]Howard Hughes Medical Institute, Department of Molecular Biology,
[2]Lewis-Sigler Institute for Integrative Genomics and Joseph Henry Laboratories of Physics,
Princeton University, Princeton, NJ 08544, USA

[3]Developmental Biology Program, Sloan-Kettering Institute, 1275 York Avenue, New York, NY 10065 USA

Running title: Integrating actomyosin contractility in tissues

Character count: 40,118

Corresponding author:

Eric Wieschaus

efw@princeton.edu

Washington Road

Princeton, NJ 08544, USA

Abstract

Contractile forces generated by the actomyosin cytoskeleton within individual cells collectively generate tissue-level force during epithelial morphogenesis. During *Drosophila* mesoderm invagination, pulsed actomyosin meshwork contractions and a ratchet-like stabilization of cell shape drive apical constriction. Here, we investigate how contractile forces are integrated across the tissue. Reducing adherens junction (AJ) levels or ablating actomyosin meshworks causes tissue-wide epithelial tears, which release tension that is predominantly oriented along the anterior-posterior (a-p) embryonic axis. Epithelial tears allow cells normally elongated along the a-p axis to constrict isotropically, suggesting that apical constriction generates anisotropic epithelial tension that feeds-back to control cell shape. Epithelial tension requires the transcription factor Twist, which stabilizes apical myosin II, promoting the formation of a supracellular actomyosin meshwork in which radial actomyosin fibers are joined end-to-end at spot AJs. Thus, pulsed actomyosin contractions require a supracellular, tensile meshwork to transmit cellular forces to the tissue-level during morphogenesis.

Introduction

Throughout development, epithelial sheets of cells undergo dramatic rearrangements, such as tissue folding and invagination, to generate complex three-dimensional organs in a process called epithelial morphogenesis (Lecuit and Lenne, 2007; Leptin, 2005; Quintin et al., 2008). Epithelial morphogenesis results from coordinated cell shape changes and movements that collectively deform tissues (Gustafson and Wolpert, 1962; Holtfreter, 1943; Shih and Keller, 1992; Sweeton et al., 1991). Individual cell shape changes and movements require that forces are generated within cells. In addition, for cellular forces to result in coherent changes in tissue architecture, forces must be transmitted between epithelial cells. The mechanical coupling of epithelial cells implies that the integration of cellular forces can in turn influence individual cell dynamics (Gorfinkiel et al., 2009; Peralta et al., 2007; Pouille et al., 2009; Solon et al., 2009). Therefore, understanding tissue morphogenesis requires determining how cellular forces are integrated across tissues and whether tissue-level forces feedback to control individual cell behaviors.

A common cell shape change that results in epithelial morphogenesis is apical constriction. Apical constriction reduces the apical cross-sectional area of an epithelial cell, which transforms a columnar cell to a wedge or cone shape. Coordinated apical constriction of mechanically coupled cells promotes epithelial folding and tissue invagination (Odell et al., 1981). During *Drosophila* gastrulation, apical constriction appears to be required for the invagination of the prospective mesoderm, a strip of ~1200 cells along the ventral midline of the embryo (Leptin and Grunewald, 1990; Parks and Wieschaus, 1991; Sweeton et al., 1991). Apical constriction of mesoderm cells is polarized, or anisotropic, such that cells constrict predominantly in the ventral-lateral (v-l) direction, remaining longer along the anterior-posterior

(a-p) axis (Sweeton et al., 1991) (Figure 1A). The mechanism responsible for anisotropic constriction is not known, but one consequence is that while the tissue contracts in the v-l direction, a-p tissue length remains relatively constant, resulting in a long, narrow ventral furrow.

Understanding the cause of anisotropy requires elucidating the mechanisms of force generation in cells and tissues. In ventral furrow cells, apical constriction is driven by pulsed contractions of an actomyosin meshwork that spans the apical cortex and is coupled to the cell surface via AJs (Dawes-Hoang et al., 2005; Martin et al., 2009; Sawyer et al., 2009). Between contractions, the constricted state of the cell is stabilized such that cells constrict incrementally via a ratchet-like mechanism (Martin et al., 2009). Anisotropic constriction in ventral furrow cells could thus result from an individual cell behavior, if for example force generation during contraction pulses was directional.

Alternatively, anisotropic constriction could reflect mechanical constraints on individual cell constriction imposed by the mechanical properties of the tissue (Hardin and Keller, 1988), such as greater tension along the a-p axis. Actomyosin contractility associated with apical constriction likely generates epithelial tension, however, it is unclear how tension is directed across the mesoderm primordium. Furthermore, how pulsatile and stable contractile forces contribute to the global mechanical properties of the tissue is unknown. In this study, we combine live imaging, computational image analysis, laser ablation, and genetics to examine the influence of tissue mechanics on individual cell shape changes and the mechanisms by which cellular forces are transmitted across the tissue.

Results

Anisotropic apical constriction possibly reflects tissue mechanics

Polarized constriction could result from an individual cell behavior, such as directional actomyosin-based force generation along the v-l axis. Alternatively, a mechanical property of the tissue, such as greater tension along the a-p axis, could bias the direction in which cells constrict. Because ventral furrow cell apical constriction is pulsed (Martin et al., 2009), we decided to distinguish between these possibilities by determining whether the increase in cell polarization correlates with pulses of actomyosin contraction in individual cells. To visualize apical cell shape, we imaged ventral furrow cells in live embryos expressing the membrane markers Spider-GFP and Resille-GFP (Morin et al., 2001). We quantified the polarization of apical constriction by fitting apical cell outlines with ellipses and measuring two parameters (Figure 1B). Cell aspect ratio, which is independent of the orientation to the a-p axis (θ), was measured by dividing the major axis of the fitted ellipse (a) by the minor axis (b). In addition, we measured cell "anisotropy" relative to the embryonic axis by dividing the cell's length along the a-p axis (x) by the cell's length along the v-l axis (y). Aspect ratio and anisotropy had similar values in elongated cells during furrow formation because cells were aligned along the a-p axis such that $\theta \sim 0$ (data not shown). Mean anisotropy and aspect ratio gradually increased to ~ 2 before cells invaginated into the embryo interior (Figure 1C and D). Analysis of individual cells demonstrated that transient increases in anisotropy did sometimes coincide with contraction pulses (Figure 1E and F, i). However, anisotropy also increased between contractions (Figure 1E and F, ii). Overall, there was not a strong correlation between constriction rate and the rate of change in anisotropy ($r = 0.1 \pm 0.24$, n = 125 cells, 3 embryos), suggesting that directional contraction of individual cells is not solely responsible for the anisotropy. Furthermore,

anisotropic constriction still occurred in *bicoid nanos torso-like* (*bnt*) embryos that lack a-p polarity, demonstrating that directional information for individual cell constriction is not provided by the a-p patterning system (Figure 1D). These results suggest that rather than being caused by discrete cellular behaviors, anisotropic apical constriction could result from the global mechanics of the tissue.

AJs integrate contractile forces to generate epithelial tension

AJs, which contain complexes of the transmembrane adhesion molecule E-cadherin and the adaptors β-catenin and α-catenin, link neighboring cells to each other and the cell surface to the actin cortex (Gumbiner, 2005). Partial loss-of-function mutants in the *Drosophila* β-catenin (Armadillo or Arm), such as arm^{043A01}, result in lower levels of Arm, E-cadherin, and α-catenin at the cell surface (Cox et al., 1996; Sawyer et al., 2009; Sokac and Wieschaus, 2008). Therefore, to determine whether there are mechanical properties of the ventral furrow that might explain cell anisotropy, we examined the consequences of reducing AJ levels using maternal and zygotic arm^{043A01} mutants ($arm^{M/Z}$). Because contractile forces for apical constriction are generated by myosin II on the apical surface, we first visualized apical Myosin-GFP in live $arm^{M/Z}$ embryos. In wild-type embryos myosin II forms a meshwork on the ventral surface of the embryo (Martin et al., 2009) (Figure 2A, Supplemental Video 1). In some $arm^{M/Z}$ embryos (n = 4/11), myosin II structures uniformly dissociated across the tissue, presumably due to a global lack of cell adhesion (data not shown). However, in the majority of $arm^{M/Z}$ embryos (n = 7/11), the myosin II meshwork remained locally intact, but tore across the entire width of the ventral furrow at apparently random positions along the a-p axis before completely dissociating (Figure 2A, Supplemental Video 1). Myosin-GFP in the adjacent tissue retracted away from the tear,

widening the gap in the myosin II meshwork (Figure 2B). Epithelial tears occurred in the ventral furrow, but were not observed in more lateral ectoderm at the same stage (data not shown). These results suggest that apical constriction of ventral furrow cells generates epithelial tension, which can disrupt cell-cell adhesion in embryos with weakened AJs. Similar epithelial tears and tissue retractions were observed when *arm* (23/24 *armRNAi* embryos), E-cadherin (10/12 *ECad2RNAi* embryos) or α-catenin (3/12 *α-cateninRNAi* embryos) expression was knocked-down using RNAi, demonstrating that all core AJ components are required for epithelial tension (Supplemental Figure 1A, 1B). However, the most striking feature of these tears was that the associated tissue retraction was always directed along the a-p axis of the embryo. This suggests that epithelial tension transmitted through AJs is highest along the a-p axis during ventral furrow formation, which could explain the observed cell anisotropy.

Epithelial tension is highest along the length of the ventral furrow

It was possible that decreasing the levels of AJ proteins changed the wild-type distribution of tensile forces present in the mesoderm primordium. Therefore, we sought to test whether tension is anisotropic in this tissue using an independent approach. Laser ablation has served as an excellent method to measure relative tensile forces in epithelial tissues undergoing morphogenesis (Kiehart et al., 2000). Targeted ultraviolet (UV) laser irradiation severs actin and myosin II containing structures, resulting in the recoil of the surrounding tissue whose initial velocity (displacement/time) immediately after ablation is proportional to the magnitude of the resting tension (Fernandez-Gonzalez et al., 2009; Hutson et al., 2003). Because tissue retraction associated with local ablations could be influenced by the orientation of cellular actomyosin structures, we first made 20 μm-long, multicellular laser incisions along either the a-p or v-l axes

and measured the initial myosin II displacement perpendicular to the incision at various distances from the incision (Figure 3A). Incisions across the width of the ventral furrow resulted in dramatic myosin displacement all along the a-p axis of the embryo (D_{ap}), indicating tension along this axis (Figure 3B, Supplemental Video 2). Laser incisions parallel to the furrow resulted in significantly less displacement along the v-l axis (D_{vl}) (Figure 3B, Supplemental Video 2), consistent with there being lower v-l tension. To more accurately measure the initial velocity of tissue retraction, we also performed 1 μm point ablations in which we imaged myosin II displacement within 3 seconds of initiating ablation (compared to 9 seconds for line ablation, Supplemental Figure 2). Ablation of isometric-looking myosin structures resulted in retraction of the surrounding tissue (Figure 3D). To determine if this displacement was directional, we measured the initial radial displacement of myosin structures (D_r) from the site of ablation at different angles (θ) representing different directions relative to the a-p and v-l axes (Figure 3E). The initial radial displacement in wild-type embryos was 2-3–fold higher along the a-p axis of the embryo (Figure 3F). These results confirm the conclusions from our analysis of $arm^{M/Z}$ mutants and demonstrate that epithelial tension is predominantly directed along the length of the ventral furrow.

Epithelial tension along the a-p axis causes anisotropic apical constriction

The higher tension along the a-p axis suggests the possibility that ventral furrow cells attempt to constrict isotropically, but encounter more resistance and thus constrict less along the a-p axis. To determine whether epithelial tension biases constriction to occur in the v-l direction, we examined how the disruption of epithelial tension that results from AJ depletion affects cell shape change in both live and fixed embryos. In *armRNAi* embryos, cells within the tear rapidly

expanded after dissociation of myosin II structures (Figure 4A and B, Supplemental Video 3). These distended cells abnormally changed neighbors as they expanded, suggesting that they had lost adhesion to one another (Figure 4C). Simultaneous with local cell expansion in the tear, the surrounding cells appeared to lose their a-p polarization and underwent isotropic apical constriction (Figure 4A and 4D, Supplemental Video 3). In live *armRNAi* embryos, cells that constricted after a neighboring epithelial tear exhibited a mean anisotropy of 1.07 ± 0.27 (mean ± s.d., n = 120 cells, 3 embryos), close to being perfectly isotropic (anisotropy = 1). Furthermore, we observed cases in live *armRNAi* and *ECad2RNAi* embryos where cells began to constrict anisotropically and then became more isotropic after epithelial tearing events (Figure 4D, E, F). These results strongly suggest that individual cells are not hard-wired to undergo polarized contraction, but that apical constriction generates higher epithelial tension along the a-p axis, providing a mechanical constraint that feeds-back to control the resulting individual cell shape.

Actomyosin fibers connected by spot AJs form a supracellular meshwork

We next examined how contractile forces are transmitted across the tissue. The epithelial tears in $arm^{M/Z}$ embryos suggested that apical actomyosin meshworks are coupled to each other through AJs. Therefore, we examined how cytoskeletal structures are linked between cells during ventral furrow formation using fixed embryos labeled with myosin II, actin, and E-cadherin. Before furrow formation, the majority of myosin II was present as isolated spots on the apical surface of individual cells, the largest of which likely resulted from pulses of myosin II coalescence (Figure 5A). As myosin II levels increased and a furrow developed, myosin II and actin formed supracellular fibers that extended across multiple cells and were incorporated into the tissue-wide meshwork (Figure 5A and 5B). Supracellular actomyosin fibers bridged the

apical surface of the cell, such that the ends of myosin II fibers met at cell-cell interfaces (Figure 5B, i). Multiple radial actomyosin fibers often originated from a central myosin II spot or ring, which formed branches in the tissue-wide meshwork (Figure 5B, i). In addition to radial actomyosin fibers, some supracellular actomyosin fibers ran along cell boundaries (Figure 5B, ii). In ventral furrow cells, subapical adherens junctions ~ 4 μm below the apical cortex are disassembled and reappear at the apical surface as spot-like structures between cell vertices (Dawes-Hoang et al., 2005; Kölsch et al., 2007; Martin et al., 2009) (Figure 5C). Spot AJs appeared to connect radial actomyosin fibers end-to-end to generate the supracellular fibers (Figure 5C). Interestingly, spot AJs linking actomyosin fibers were often stretched along the fiber, possibly indicating tension being exerted on the junction (Figure 5C). Thus, spot AJs appear to integrate cellular actomyosin networks into supracellular actomyosin fibers, resulting in a tissue-wide actomyosin meshwork.

Spot AJs transmit tension from actomyosin fibers across the plasma membrane

To test whether spot AJs transmit tension between cellular actomyosin fibers, we examined more closely the cellular organization and dynamics of myosin II in embryos with reduced AJs. Supracellular actomyosin fibers initially formed in $arm^{M/Z}$ embryos, consistent with this allele retaining partial function (Figure 2A). However, upon epithelial tearing myosin II fibers rapidly contracted, demonstrating that myosin II fibers generate contractile force in a manner similar to stress fibers (Kumar et al., 2006) (Figure 2C, i, Supplemental Video 4). Loss of cell adhesion resulted in myosin II contraction into rings or balls across the entire epithelium (Figure 2A and 2C, ii and iii, Figure 4A and B). Myosin II spots continuously flowed into myosin II rings, suggesting that unrestrained actomyosin contraction occurs in the absence of

opposing contractile forces from surrounding cells (Figure 2C, iii, Supplemental Video 5). These results suggest that spot AJs balance tensile forces generated by cellular actomyosin networks to allow the formation of stable actomyosin fibers that transmit tension across the tissue.

The retraction of actomyosin fibers in embryos with reduced AJs could reflect a disruption of the extracellular linkage between adjacent cell plasma membranes or the intracellular connection between the plasma membrane and the actomyosin cortex. To distinguish between these models, we examined whether cell membranes completely separate during tearing events using scanning electron microscopy (SEM). In the ventral furrow of wild-type embryos, boundaries between cells cannot be discerned because of tight adhesion of these cells through apical AJs (Figure 6A). In contrast, individual ventral cells can easily be identified in $arm^{M/Z}$ mutants because cells lose tight adhesion to one another, specifically in the ventral furrow region (Figure 6B). In addition, we identified tearing events in which adjacent rows of cells became separated (Figure 6C). SEM demonstrated that the cell expansion observed using confocal microscopy represented cells rounding up upon loss of adhesion. Consistent with the global contraction of the surrounding tissue in live embryos, the isotropically constricting cells adjacent to the tear contained dramatic membrane blebs, suggesting that the apical cortex rapidly contracts upon loss of epithelial tension across the tissue.

Despite the dramatic loss of adhesion, cells in $arm^{M/Z}$ embryos maintained thin membrane connections, or tethers, to their neighbors (Figure 6B and C). Live imaging of the apical surface during tearing events demonstrated that membrane tethers form as cell apices contract away from each other (Supplemental Video 6). Membrane tethers remained connected to clusters of membrane blebs, which colocalized with myosin II rings and some remaining cortical E-cadherin

(Figure 6D, Supplemental Figure 1C). Tethers often contained detectable levels of F-actin, but not myosin II, suggesting that tethers fail to transmit tension (Supplemental Figure 1D). We propose that membrane tethers form when the actomyosin cortex detaches from the one side of a fiber-AJ-fiber connection (Figure 6E). This detachment did not indicate a specific function for β-catenin in coupling the actomyosin cortex to AJs since membrane tethers were also observed in both *α-cateninRNAi* and *ECad2RNAi* embryos (Supplemental Figure 1E). Thus, reducing the number of AJs possibly focuses the large amount of contractile force generated by ventral furrow cells onto the few remaining AJ-cytoskeleton connections, exceeding the forces of adhesion and causing junctions to detach from the tensile meshwork. However, because we have been unable to completely disrupt AJs, we cannot rule out the possibility that membrane tethers result from cell-cell adhesion that is E-cadherin and Arm independent. Regardless of the exact nature of the membrane connection, tether formation upon disruption of AJs further argues that spot AJs balance contractile forces across the plasma membrane, allowing tension to be transmitted between cells.

Epithelial tears and loss of cell-cell adhesion fail to occur in the absence of Snail-mediated actomyosin contraction

We have hypothesized that the epithelial tears observed in embryos with disrupted AJs result from contractility of the supracellular actomyosin meshwork. We previously showed that the transcription factor Snail is required for pulsed contractions and apical actomyosin meshwork assembly (Martin et al., 2009). Therefore, we determined whether Snail is required for the epithelial tears and loss of cell adhesion observed in *arm* mutant embryos by performing double RNAi experiments in which the expression of *sna* was reduced in combination with *arm*. A

control dsRNA (*CG3651RNAi*) had no effect on its own or with *armRNAi* (Figure 7A, Supplemental Video 7), demonstrating that multiple dsRNAs can be combined without affecting the potency of RNAi. Knock-down of *sna* and *arm* suppressed the formation of epithelial tears and the loss of adhesion normally observed in *armRNAi* embryos (n = 5 embryos) (Figure 7A, Supplemental Video 8). In addition, *snaRNAi* suppressed apical myosin II recruitment and contraction into rings in *armRNAi* embryos. Thus, epithelial tearing and loss of cell adhesion fail to occur in the absence of Snail-mediated actomyosin assembly, supporting the model that tension generated by the actomyosin contraction is responsible for these phenotypes.

Twist-mediated stabilization is required to transmit epithelial tension

The transcription factor Twist affects actomyosin contractility in the ventral furrow differently than Snail. Pulses of actomyosin contraction still occur in *twi* mutant and *twiRNAi* embryos. However, the resulting constriction fails to be stabilized, possibly due to a defect in maintaining cortical tension (Martin et al., 2009). Therefore, we examined whether Twist is required for the epithelial tears in *armRNAi* embryos to distinguish the roles of pulsed actomyosin contraction and Twist-dependent stabilization in generating tissue-wide epithelial tension. Pulses of myosin II coalescence occurred in *twi-armRNAi* embryos, similar to *twiRNAi* alone (Figure 7A, Supplemental Video 9). Similar to *armRNAi* embryos, cells lost adhesion and formed tethers and dramatic blebs in *twi-armRNAi* embryos. Thus, pulsed contractions generate local tension that can disrupt cell-cell adhesion (Figure 7B, Supplemental Figure 1F). Pulses continued even after cells lost adhesion, suggesting the pulsed contraction does not require mechanical interactions between cells. Importantly, cell dissociation occurred without the formation of tissue-wide tears along the a-p axis of the embryo (n = 10 embryos) (Figure 7A, 7B,

Supplemental Video 9 and 10), suggesting that pulsed actomyosin contractions are insufficient to generate global epithelial tension. To further examine Twist's role in generating tension, we performed laser incisions across the width of the furrow and measured a-p myosin displacement (D_{ap}) in control (H_2O injected) and *twiRNAi* embryos. *twiRNAi* embryos exhibited significantly lower levels of recoil at all distances from the incision, demonstrating that Twist is indeed required to transmit tension between ventral furrow cells (Figure 3C). Because Twist enhances Snail expression, it was possible that the disruption of epithelial tension was due to lower levels of Snail activity (Kosman et al., 1991; Leptin, 1991). However, knock-down of the two Twist targets, *fog* and *t48* (Costa et al., 1994; Kölsch et al., 2007), also suppressed the formation of tissue-wide epithelial tears in *fog-t48-armRNAi* embryos, demonstrating that this Twist activity is independent of Snail (data not shown). Consistent with the importance of Twist in generating tissue-wide tears, epithelial tears in $arm^{M/Z}$ mutants are restricted to ~ 14 cells within the 18 cell-wide Snail expression domain (Figure 7C), corresponding to the domain of highest Twist expression, where transcriptional targets such as *folded gastrulation* are activated (Costa et al., 1994; Leptin, 1991). Thus, Twist-mediated stabilization is required to transmit tension across the tissue, which is required for epithelial tears in *arm* mutant embryos.

Twist stabilizes apical myosin II fibers between contraction pulses to form a supracellular actomyosin meshwork

Why do pulsed myosin II contractions in *twiRNAi* embryos fail to transmit tension across the tissue? To address this question, we used Myosin-GFP and Membrane-mCherry to compare cellular myosin II dynamics in wild-type and *twiRNAi* embryos. In wild-type cells, myosin II fibers remain on the apical cortex after contraction pulses during the stabilization phase of apical

constriction (Martin et al., 2009) (Figure 8A). This results in a gradual increase in cortical myosin II levels over a series of contractions (Figure 8B). In contrast, myosin II seemed to disappear from the apical cortex after contraction pulses in *twiRNAi* embryos, with myosin II levels falling back to near the same level as before the pulse (Figure 8A and 8B). To determine whether *twiRNAi* affects cortical myosin II levels after contraction, we averaged normalized myosin II intensity profiles for individual pulses in control (*CG3651RNAi*) and *twiRNAi* embryos. We found that average cortical myosin II intensity in *twiRNAi* embryos dropped to a significantly lower level after a contraction pulse than control embryos (Figure 8C, $p<0.0001$). This Twist-dependent stabilization of cortical myosin II was even more dramatic in *arm-twiRNAi* embryos. In contrast to *armRNAi* embryos, where myosin II contracts into a stable cortical ring in each cell, myosin contractions in *arm-twiRNAi* embryos were pulsed, with myosin II disappearing from the cortex after coalescing (Figure 8D). Myosin II dynamics in *arm-twiRNAi* embryos were indistinguishable from *fog-t48-armRNAi* (n = 5 embryos), demonstrating that destabilization of cortical myosin II resulted directly from loss-of-function in the Twist pathway, and not from lower Snail activity (Figure 8D). Given that contraction pulses are asynchronous in adjacent cells (Martin et al., 2009), we hypothesized that the failure to retain cortical myosin II between pulses would disrupt supracellular meshwork formation since only a subset of cells would have cortical myosin II at a given time. To test this, we segmented Myosin-GFP images from control and *twiRNAi* embryos and measured the area of the largest Myosin-GFP structure at each time-point (Figure 8E). With our segmentation threshold, control embryos assembled large myosin II networks on the order of 200 – 300 μm^2, or the size of several cells (Figure 8F). However, *twiRNAi* embryos rarely exhibited myosin II networks larger than 50 μm^2, which corresponds to the apical area of an individual cell. We propose that Twist-dependent

stabilization of apical myosin II fibers is required to form the supracellular actomyosin meshwork, which allows tension to be stably transmitted across the epithelium during ventral furrow formation.

Discussion

AJs integrate tensile force along the length of the ventral furrow

Recent studies have demonstrated the importance of actomyosin and AJs for individual cell shape changes and morphogenesis (Bertet et al., 2004; Blankenship et al., 2006; Dawes-Hoang et al., 2005; Franke et al., 2005; Gorfinkiel and Arias, 2007; Martin et al., 2009; Sawyer et al., 2009). However, less is known about the underlying mechanisms by which dynamic contractile forces are transmitted between cells of an epithelium and the resulting tissue mechanics. In this study, we examined the mechanics of ventral furrow formation both by lowering AJ levels and by ablating the apical actomyosin meshwork. Reducing AJ levels sensitized cell adhesion to stress, resulting in discrete, tissue-wide epithelial tears. We propose that tears in AJ depleted embryos result from the loss of mechanical connections between cells when contractility exceeds the forces of adhesion. Interestingly, tears resulted from tissue separation along the a-p axis, suggesting that tension transmitted by AJs is mostly oriented along the length of the ventral furrow (Figure 9A). We confirmed this anisotropy in epithelial tension by showing that laser ablations in the ventral furrow also result in preferential actomyosin retraction along the a-p axis. The global a-p retraction of the surrounding tissue following epithelial tearing suggests that the ventral furrow is a mechanically coherent epithelium, in which high levels of tensile force are integrated along the length of the furrow.

It is surprising that the vast majority of the epithelial tension generated by apical constriction is oriented along the length of the furrow, the axis with the least tissue movement. Indeed, one might have expected greater levels of tension along the v-l axis given that apical constriction is thought to pull lateral cells towards the ventral midline around the circumference

of the embryo (Figure 9A). Future experiments are required to determine how anisotropic tension in the ventral furrow contributes to the bending and invagination of this epithelium.

Epithelial tension controls individual cell shape

Ventral furrow cells undergo polarized apical constriction, constricting predominantly in the v-l direction and remaining longer along the a-p axis (Sweeton et al., 1991). Because we failed to find a correlation between contraction pulses and cell anisotropy and because epithelial tension itself is anisotropic, we tested whether polarized apical constriction results from the mechanical constraints of the tissue. Indeed, epithelial tears allowed adjacent anisotropic cells to constrict isotropically, suggesting that ventral furrow cells attempt to constrict isotropically, but encounter greater resistance to constriction along the a-p axis (Figure 9B). During germband extension, tension generated by supracellular actomyosin cables influences myosin II assembly and dynamics within these cables (Fernandez-Gonzalez et al., 2009). Tension also appears to modulate actomyosin organization in the ventral furrow because epithelial tears resulted in unrestrained myosin II contraction into ring-like structures as opposed to formation of a fibrous meshwork. Thus, the coupling of cellular contractile meshworks generates tension that feeds-back to regulate both cytoskeletal organization/dynamics and cell shape. These results illustrate how the interplay between cell and tissue-level forces influences cell shape change during morphogenesis.

Spot AJs transmit tensile forces oriented perpendicular to cell interfaces

Epithelial tension observed during ventral furrow formation likely resulted from contractile forces generated by apical actomyosin meshworks. We found that cellular

actomyosin fibers were coupled end-to-end at spot AJs to form supracellular fibers and a tissue-wide meshwork. Disruption of AJs caused an imbalance of forces across the plasma membrane, resulting in membrane tethers. This supports a model in which tensile forces are integrated through discrete AJ anchors that link actomyosin networks in adjacent cells (Figure 9C). Supracellular actomyosin cables that transmit tension parallel to cell interfaces have been observed during germband extension, dorsal closure, and compartment boundary formation (Fernandez-Gonzalez et al., 2009; Landsberg et al., 2009; Rauzi et al., 2008; Rodriguez-Diaz et al., 2008). However, in the ventral furrow, supracellular actomyosin fibers are mostly oriented perpendicular to cell interfaces (Figure 9C). This orientation is similar to that of actin in forming cultured epithelia, where radial actin fibers terminate in spot junctions and form supracellular actin meshworks across the apical surface of epithelia (Adams et al., 1996; Vaezi et al., 2002; Yonemura et al., 1995). Furthermore, actin meshworks consisting of radial actin fibers emanating from central actin spots are also observed in *Xenopus* cells undergoing convergence and extension (Rolo et al., 2009; Skoglund et al., 2008). Actomyosin organization as a two-dimensional branched meshwork could represent a different mechanical paradigm for epithelial morphogenesis that enables cells to form a mechanically coherent sheet in which tensile forces are not restricted to cell interfaces, but bridge the surface of cells across the entire tissue.

Pulsatile and stable contractile networks cooperate to change cell shape and transmit tension across the tissue

Knock-down of the transcription factor Twist using RNAi separates the activities of pulsatile actomyosin contraction and cell shape stabilization between contractions (Martin et al., 2009). Pulses of actomyosin contraction continued to occur in both *twiRNAi* and *arm-twiRNAi*

embryos. In *arm-twiRNAi* embryos, pulsed contractions disrupted cell-cell adhesion and formed membrane tethers, suggesting that pulsed contractions generate cellular tension that can separate the actomyosin network from AJs. A recent study of amnioserosa apical constriction proposed that contraction pulses are activated by mechanical interactions (i.e. stretching) between cells (Solon et al., 2009). However, in ventral furrow cells, pulsatile actomyosin contractions occurred even after cells lost adhesion, suggesting that pulsed contractions are fundamentally cell autonomous, possibly resulting from dynamic behaviors of cytoskeletal networks (Munro et al., 2004; Paluch et al., 2005). Importantly, our data also showed that pulsed contractions were insufficient to generate epithelial tears. Thus, an additional mechanism is required to translate pulsatile contractile forces and cell shape changes into tissue-wide epithelial tension.

Twist-mediated stabilization is critical to transmit cellular forces to the tissue-level. We show here that Twist was required for apical myosin II fibers to remain on the apical cortex between contraction pulses. These actomyosin fibers bridging the apical cortex likely stabilize the cell apex, preventing previously observed stretching events that would dissipate force transmission across the tissue (Martin et al., 2009). Furthermore, Twist-dependent myosin II stabilization allowed the formation of the supracellular actomyosin meshwork, which was critical for generating tissue-wide tension. We propose that this actomyosin meshwork results in a mechanically integrated tissue, allowing propagation of both pulsatile and stable tensile forces (Figure 9C). Thus, while pulsed contractions generate dramatic changes in individual cell shape, stabilizing tension produced by the supracellular actomyosin meshwork transmits these contractile forces to the tissue-level, generating epithelial tension.

Pulsatile and stable contractile forces also cooperate to contract the amnioserosa during dorsal closure (Solon et al., 2009). During dorsal closure, amnioserosa contraction is stabilized

by actomyosin cable assembly in the surrounding epidermis. However, in the ventral furrow, the machinery responsible for pulsation and stabilization are both present in the mesoderm. Future studies are needed to determine how actomyosin networks with unique properties are coordinated within the same cell. Interestingly, Twist is thought to activate G-protein coupled receptor signaling, which activates stress fiber formation in cultured cells (Buhl et al., 1995; Lin et al., 2005). Thus, Twist possibly induces actomyosin fiber assembly independent of pulsed contractions. Alternatively, pulsed contractions could bundle actomyosin meshworks to form fibers that become stabilized by Twist activity. Regardless of these different models, the cooperation of pulsatile and stable networks in morphogenetic events as diverse as epithelial invagination and sheet migration suggests that coordinated pulsation and stabilization represents a conserved mode of tissue morphogenesis.

Materials and methods

Fly stocks and genetics

The following stocks containing fluorescent fusion proteins were used: *Spider-GFP* (95-1) and *Resille-GFP* (117-2) (Morin et al., 2001), Membrane-mCherry (this study), Myosin-GFP (*sqh-GFP*) (Royou, 2002), Myosin-mCherry (*sqh-mCherry*) (Martin et al., 2009). To examine cell shape in embryos devoid of anterior-posterior polarity we used the stock *w;* Resille-GFP*; bicoid*^{E1} *nanos*^{L7} *torso-like*^{146} / TM3; Sb. We analyzed embryos from mothers that were homozygous for *bicoid*^{E1} *nanos*^{L7} *torso-like*^{146}. To generate *arm*$^{M/Z}$ mutants we created *arm*^{043A01} germline clones using the FLP-DFS system (Chou and Perrimon, 1992). We visualized myosin II in *arm*$^{M/Z}$ mutants by generating a stock that was *arm*^{043A01} *FRT101/FM7; sqh-GFP*. We crossed females of this genotype to *w ovo*^{D} *FRT101*/Y; *flp-138* males to obtain *arm*^{043A01} *FRT101/ w ovo*^{D} *FRT101*; *flp-138*/+ females. These females were heat shocked as larvae for 2 hr at 37°C each day to induce mitotic recombination in the germline. We imaged embryos from the following cross: *arm*^{043A01} *FRT101/ w ovo*^{D} *FRT101*; *flp-138*/+ females x FM7/+; *flp-138*/+ males. Half of these embryos showed the mutant phenotype described in the paper, consistent with half being rescued zygotically.

Construction of Membrane-mCherry

A Membrane-mCherry marker was created by fusing the N-terminal 20 amino acids of the rat Gap43 gene, which contains a myristoylation sequence, to mCherry. This Membrane-mCherry fusion was cloned into a pBluescript vector containing the *sqh* promoter and 3' untranslated region (Martin et al., 2009). The 3-kilobase KpnI/XbaI *sqh5'*-Membrane::mCherry-*sqh3'* fragment was then inserted into a transformation vector containing the attB site (pTiger,

courtesy of Scott Ferguson, SUNY Fredonia). The resulting construct was sent to Genetic Services Inc. for integration into the attP2 site using the phiC31 integrase system (Groth et al., 2004).

Live cell imaging

To prepare embryos for live imaging, embryos were dechorionated with 50 % bleach, washed with water, and mounted ventral side up on a slide covered with embryo glue (Scotch tape resuspended in heptane) between two No. 1.5 coverslip spacers. A coverslip was placed over the embryo and Halocarbon 27 oil was added to the resulting chamber. The spacers prevented the overlying coverslip from contacting the ventral surface of the embryo such that the embryo was not compressed. Embryos imaged under these conditions developed normally and subsequently hatch, demonstrating that our imaging conditions had minimal impact on development. All imaging was done in Halocarbon 27 oil at room temperature (~ 23°C).

Spider-GFP, *Resille-GFP*, *sqh-mCherry*;*Spider-GFP*, and *sqh-GFP*; Membrane-mCherry videos were obtained with a Leica SP5 confocal microscope, a 63x/1.3 numerical aperture glycerine-immersion objective (Leica), an argon ion laser and a 561 nm diode laser. Images were acquired using a pinhole setting from 1-2 Airy Units. For multichannel imaging, we set the excitation bandpass to 495 – 550 nm to detect GFP and 578 – 650 nm to detect mCherry. *sqh*-GFP single-channel videos were obtained using the aforementioned imaging system or with a PerkinElmer Ultraview spinning disk confocal microscope controlled with Volocity Acquisition software (Improvision), a 60x/1.4 numerical aperture oil-immersion objective (Nikon), an argon/krypton laser, and an EMCCD camera (Hamamatsu, Model C9100-13).

Laser ablation

Embryos were prepared for live imaging as described above and were imaged using a PerkinElmer Ultraview spinning disk confocal equipped with a 63x/1.4 numerical aperture oil immersion lens controlled with Metamorph software (Universal Imaging). A N_2 Micropoint laser (Photonics Instruments) tuned to 365 nm was focused on *sqh-GFP* structures on the ventral surface of the embryo to ablate actomyosin structures. Point ablations were performed by ablating isotropic *sqh-GFP* spots with a point of ~ 1 μm diameter, which took ~ 670 ms. Line ablations were performed by making 9 sequential point ablations to make a 20 μm incision, which took ~ 6.4 s. Z-stacks were acquired immediately preceding and following ablation in order to measure displacement of myosin II structures upon release of tension.

Image processing and analysis

Images presented were processed using ImageJ (http://rsb.info.nih.gov/ij/) and Photoshop CS (Adobe Systems, Inc.). A Gaussian smoothing filter with a radius of one pixel was used to reduce noise in published images. Myosin II images presented in all figures are maximum intensity Z-projections of the apical ~ 5 μm of cells in the middle of the image. Because myosin II is almost entirely present on the apical surface of cells, these images represent a surface projection of the embryo. Images of cell outlines are Z-slices ~ 2 μm below the apical surface.

Image segmentation was performed using custom MATLAB (MathWorks) software. Raw images were bandpass filtered with effective cutoff wavelengths of ~ 1.4 μm (low pass) and ~ 16 μm (high pass). Images were then thresholded and skeletonized to reduce the width of the membranes to one pixel. Cells were then indexed and tracked based on the distance between cell centroids at subsequent time points. We manually removed cells with errors in the segmentation

to ensure that all cells in the dataset were correctly identified. Aspect ratio and anisotropy were calculated by using the 'regionprops' function in MATLAB to measure major axis length, minor axis length, and orientation for individual cells. We measured the intensity of cortical myosin II in individual cells using 3-dimensional time-lapse videos that were ~ 5 μm in depth. To separate cortical myosin II structures from the diffuse cytoplasmic staining, we smoothed *sqh-GFP* images using a Gaussian smoothing filter with a three-pixel kernel size and sigma = 0.5 pixels and clipped intensity values three standard deviations above the mean. We then made maximum-intensity Z-projections of myosin II (averaging the two highest intensity values) and integrated the intensity of all the pixels in a given cell. Data for apical area, myosin intensity, and anisotropy were smoothed using a Gaussian smoothing filter (sigma = 18-24 s, 3 time points) to remove noise.

Recoil of *sqh-GFP* structures following laser ablation was quantified using custom software in which myosin spots were hand selected and tracked from the pre-ablation frame to the post-ablation frame (Fernandez-Gonzalez et al., 2009).

To measure the continuity of the supracellular meshwork in control injected and *twiRNAi* embryos, we thresholded maximum intensity projections of *sqh-GFP* images using the mean pixel intensity as a cutoff. We then used the 'bwmorph' function in MATLAB to identify connected objects and identified the largest object at each time-point in a time-lapse video.

Embryo fixation and staining

To visualize cytoskeletal structures, embryos were fixed with 8 % paraformaldehyde/heptane for 30 minutes, manually devitellinized, stained, and mounted in AquaPolymount (Polysciences, Inc.). Endogenous *sqh-GFP* fluorescence was used to visualize

myosin II and Alexa-568 phalloidin (Molecular Probes) was used to visualize F-actin. *Drosophila* E-Cadherin (DCad2) was recognized using rat anti-DCad2 (Developmental Studies Hybridoma Bank) at a dilution of 1:50. Snail and Neurotactin double stainings were performed in heat-fixed embryos using mouse anti-Neurotactin (BP106, Developmental Studies) and rabbit anti-Snail (a gift from Mark Biggin) at dilutions of 1:100 and 1:1000, respectively.

Scanning electron microscopy

Embryos were dechorionated with 50% bleach and fixed for 25 minutes at room temperature (23°C) with a 1:1 mixture of 25% gluteraldehyde in 0.1 M Cacodylate buffer and heptane. The vitelline membrane was then manually removed with a needle and embryos were dehydrated by gradually stepping up the concentration of ethanol (25%, 50%, 75%, 95%, 100%). Embryos were then incubated for 10 minutes with a 1:1 mixture of ethanol and Tetramethylsilane (TMS) and then with 100% TMS. The TMS was allowed to evaporate and we transferred the embryos to the microscope stand and performed metal coating using a Denton Vacuum Desk II Sputterer. Samples were imaged using a tabletop TM-1000 scanning electron microscope from Hitachi.

RNAi

Primers for dsRNA were designed with E-RNAi (Arziman et al., 2005). Primers included the sequence of the T7 promoter (5'-TAATACGACTCACTATAGGGAGACCAC-3') followed by the following recognition sequences: Arm-F, 5'-CCTGGTTACCATAGGCCAGA-3'; Arm-R, 5'- TGCCATCTCTAACAGCAACG-3'; ECad2-F, 5'-GAGAGGAGGCAACAGAAACG-3'; ECad2-R, 5'-GGACATACTCTCTAGCGGCG-3';

Alpha-catenin-F, 5'-AAGCTGCAAAATCGGGTAATGAAAA-3', Alpha-catenin-R, 5'-TCTAAGACTCGTTTGGTGTAAATAC-3'; Fog-F, 5'- TGGTGACCAGTTCTCTTTCC-3'; Fog-R, 5'- TGTTGCAGTTGCCGAAGT-3'; T48-F, 5'- CCGCCGGCTACTTGGA-3'; T48-R, 5'- GAAAGAAGTCGATAAGCTGG-3'. For *twistRNAi, snaRNAi*, and control *CG3651RNAi*, we used the Twi01, Sna01, and control primer pairs (Martin et al., 2009). Primer pairs were used to amplify a PCR product from genomic DNA. PCR products were used in a transcription reaction with T7 polymerase using the MEGAscript transcription kit (Ambion). Annealing was performed by adding 10mM EDTA, 0.1% SDS, and 0.1M NaCl to the reaction and incubating this mixture in a water bath heated to above 90°C, which was allowed to cool for several hours. The dsRNA was purified by phenol/chloroform extraction and resuspended in injection buffer (5mM KCl, 0.1 mM NaPhosphate, pH 7.0). Newly laid embryos were injected laterally and incubated for 2.5-3 hours at room temperature (23°C) before imaging gastrulation. We injected adherens junction dsRNA at a concentration of ~1 mg ml^{-1}. However, tears in the myosin II network could be observed even after diluting dsRNA to lower concentration. For most experiments, Arm dsRNA was used at 0.2 mg ml^{-1}. For double RNAi experiments, Arm dsRNA was used at 0.2 mg ml^{-1} and Twist and Snail dsRNA was used at 2 mg ml^{-1}. For triple RNAi experiments, Arm dsRNA was used at 0.2 mg ml^{-1}, and Fog and T48 were used at 0.8 mg ml^{-1} and 0.65 mg ml^{-1}, respectively.

Online supplemental material

Fig. S1 shows that knock-down of E-cadherin, Arm, or α-catenin disrupts the myosin II network and results in membrane tethers. Fig. S2 shows Myosin-GFP displacement as a function of time for the two types of laser ablation experiments shown in Figure 3. Video 1 shows Myosin-GFP

in wild-type and *arm*$^{M/Z}$ mutant embryos. Video 2 shows laser ablations in Myosin-GFP embryos. Video 3 shows Myosin-mCherry and Membrane-GFP in an *armRNAi* embryo. Video 4 shows the contraction of a myosin II fiber in an *arm*$^{M/Z}$ mutant embryo. Video 5 shows the unrestrained myosin II contraction that occurs after tearing in an *armRNAi* embryo. Video 6 shows membrane tether formation in a Membrane-GFP embryo. Video 7 shows Myosin-GFP in a double RNAi control *arm-CG3651RNAi* embryo. Video 8 shows the suppression of tears and loss of cell-cell adhesion in a Myosin-GFP *arm-snaRNAi* embryo. Video 9 shows that contraction pulses continue despite loss of cell-cell adhesion in a Myosin-GFP *arm-twiRNAi* embryo. Video 10 shows the suppression of epithelial tears in a Membrane-GFP *arm-twiRNAi* embryo.

Acknowledgements

We are especially grateful to J. Zallen for allowing us to use the laser ablation system developed in her lab. We thank J. Goodhouse for his assistance with microscopy; S. Ferguson for providing the phiC31 integration vector; and A. Sokac, Y.-C. Wang, and J. Zallen for their helpful suggestions on the manuscript. This work was supported by grant PF-06-143-01-DDC from the American Cancer Society to A.C.M., P50 grant GM071508 from NIH/NIGMS to M.K., R01 grant GM079340 from NIH/NIGMS to J. Zallen, and National Institute of Child Health and Human Development grant 5R37HD15587 to E.F.W. E.F.W. is an investigator of the Howard Hughes Medical Institute.

Abreviations list

Adherens junctions (AJs), anterior-posterior (a-p), ventral-lateral (v-l), RNA interference (RNAi), scanning electron microscopy (SEM)

References

Adams, C.L., W.J. Nelson, and S.J. Smith. 1996. Quantitative analysis of cadherin-catenin-actin reorganization during development of cell-cell adhesion. *The Journal of Cell Biology*. 135:1899-911.

Arziman, Z., T. Horn, and M. Boutros. 2005. E-RNAi: a web application to design optimized RNAi constructs. *Nucleic Acids Res*. 33:W582-8.

Bertet, C., L. Sulak, and T. Lecuit. 2004. Myosin-dependent junction remodelling controls planar cell intercalation and axis elongation. *Nature*. 429:667-71.

Blankenship, J.T., S.T. Backovic, J.S. Sanny, O. Weitz, and J.A. Zallen. 2006. Multicellular rosette formation links planar cell polarity to tissue morphogenesis. *Dev Cell*. 11:459-70.

Buhl, A.M., N.L. Johnson, N. Dhanasekaran, and G.L. Johnson. 1995. G alpha 12 and G alpha 13 stimulate Rho-dependent stress fiber formation and focal adhesion assembly. *J Biol Chem*. 270:24631-4.

Chou, T.B., and N. Perrimon. 1992. Use of a yeast site-specific recombinase to produce female germline chimeras in Drosophila. *Genetics*. 131:643-53.

Costa, M., E.T. Wilson, and E. Wieschaus. 1994. A putative cell signal encoded by the folded gastrulation gene coordinates cell shape changes during Drosophila gastrulation. *Cell*. 76:1075-89.

Cox, R.T., C. Kirkpatrick, and M. Peifer. 1996. Armadillo is required for adherens junction assembly, cell polarity, and morphogenesis during Drosophila embryogenesis. *The Journal of Cell Biology*. 134:133-48.

Dawes-Hoang, R.E., K.M. Parmar, A.E. Christiansen, C.B. Phelps, A.H. Brand, and E.F. Wieschaus. 2005. folded gastrulation, cell shape change and the control of myosin localization. *Development*. 132:4165-78.

Fernandez-Gonzalez, R., M. Simoes Sde, J.C. Roper, S. Eaton, and J.A. Zallen. 2009. Myosin II dynamics are regulated by tension in intercalating cells. *Dev Cell*. 17:736-43.

Franke, J.D., R.A. Montague, and D.P. Kiehart. 2005. Nonmuscle myosin II generates forces that transmit tension and drive contraction in multiple tissues during dorsal closure. *Curr Biol*. 15:2208-21.

Gorfinkiel, N., and A.M. Arias. 2007. Requirements for adherens junction components in the interaction between epithelial tissues during dorsal closure in Drosophila. *J Cell Sci*. 120:3289-98.

Gorfinkiel, N., G. Blanchard, R. Adams, and A. Martinez Arias. 2009. Mechanical control of global cell behaviour during dorsal closure in Drosophila. *Development*. 136:1889-1898.

Groth, A.C., M. Fish, R. Nusse, and M.P. Calos. 2004. Construction of transgenic Drosophila by using the site-specific integrase from phage phiC31. *Genetics*. 166:1775-82.

Gumbiner, B.M. 2005. Regulation of cadherin-mediated adhesion in morphogenesis. *Nat Rev Mol Cell Biol*. 6:622-34.

Gustafson, T., and L. Wolpert. 1962. Cellular mechanisms in the morphogenesis of the sea urchin larva: Change in shape of cell sheets. *Experimental Cell Research*. 27:260-279.

Hardin, J., and R. Keller. 1988. The behaviour and function of bottle cells during gastrulation of Xenopus laevis. *Development*. 103:211-30.

Holtfreter, J. 1943. A study of the mechanics of gastrulation (part 1). *J. Exp. Zool.* 94:261-318.

Hutson, M.S., Y. Tokutake, M.S. Chang, J.W. Bloor, S. Venakides, D.P. Kiehart, and G.S. Edwards. 2003. Forces for morphogenesis investigated with laser microsurgery and quantitative modeling. *Science*. 300:145-9.

Kiehart, D.P., C.G. Galbraith, K.A. Edwards, W.L. Rickoll, and R.A. Montague. 2000. Multiple forces contribute to cell sheet morphogenesis for dorsal closure in Drosophila. *J Cell Biol*. 149:471-90.

Kosman, D., Y.T. Ip, M. Levine, and K. Arora. 1991. Establishment of the mesoderm-neuroectoderm boundary in the Drosophila embryo. *Science*. 254:118-22.

Kumar, S., I.Z. Maxwell, A. Heisterkamp, T.R. Polte, T.P. Lele, M. Salanga, E. Mazur, and D.E. Ingber. 2006. Viscoelastic retraction of single living stress fibers and its impact on cell shape, cytoskeletal organization, and extracellular matrix mechanics. *Biophysical Journal*. 90:3762-73.

Kölsch, V., T. Seher, G.J. Fernandez-Ballester, L. Serrano, and M. Leptin. 2007. Control of Drosophila gastrulation by apical localization of adherens junctions and RhoGEF2. *Science*. 315:384-6.

Landsberg, K.P., R. Farhadifar, J. Ranft, D. Umetsu, T.J. Widmann, T. Bittig, A. Said, F. Julicher, and C. Dahmann. 2009. Increased Cell Bond Tension Governs Cell Sorting at the Drosophila Anteroposterior Compartment Boundary. *Curr Biol*. 19:1950-5.

Lecuit, T., and P.F. Lenne. 2007. Cell surface mechanics and the control of cell shape, tissue patterns and morphogenesis. *Nat Rev Mol Cell Biol*. 8:633-44.

Leptin, M. 1991. twist and snail as positive and negative regulators during Drosophila mesoderm development. *Genes Dev*. 5:1568-76.

Leptin, M. 2005. Gastrulation movements: the logic and the nuts and bolts. *Dev Cell*. 8:305-20.

Leptin, M., and B. Grunewald. 1990. Cell shape changes during gastrulation in Drosophila. *Development*. 110:73-84.

Lin, F., D.S. Sepich, S. Chen, J. Topczewski, C. Yin, L. Solnica-Krezel, and H. Hamm. 2005. Essential roles of G{alpha}12/13 signaling in distinct cell behaviors driving zebrafish convergence and extension gastrulation movements. *The Journal of Cell Biology*. 169:777-87.

Martin, A.C., M. Kaschube, and E.F. Wieschaus. 2009. Pulsed contractions of an actin-myosin network drive apical constriction. *Nature*. 457:495-9.

Morin, X., R. Daneman, M. Zavortink, and W. Chia. 2001. A protein trap strategy to detect GFP-tagged proteins expressed from their endogenous loci in Drosophila. *Proc Natl Acad Sci U S A*. 98:15050-5.

Munro, E., J. Nance, and J.R. Priess. 2004. Cortical flows powered by asymmetrical contraction transport PAR proteins to establish and maintain anterior-posterior polarity in the early C. elegans embryo. *Dev Cell*. 7:413-24.

Odell, G.M., G. Oster, P. Alberch, and B. Burnside. 1981. The mechanical basis of morphogenesis. I. Epithelial folding and invagination. *Dev Biol*. 85:446-62.

Paluch, E., M. Piel, J. Prost, M. Bornens, and C. Sykes. 2005. Cortical actomyosin breakage triggers shape oscillations in cells and cell fragments. *Biophysical Journal*. 89:724-33.

Parks, S., and E. Wieschaus. 1991. The Drosophila gastrulation gene concertina encodes a G alpha-like protein. *Cell*. 64:447-58.

Peralta, X., Y. Toyama, M. Hutson, R. Montague, S. Venakides, D. Kiehart, and G. Edwards. 2007. Upregulation of Forces and Morphogenic Asymmetries in Dorsal Closure during Drosophila Development. *Biophysical Journal*. 92:2583-2596.

Pouille, P.A., P. Ahmadi, A.C. Brunet, and E. Farge. 2009. Mechanical signals trigger Myosin II redistribution and mesoderm invagination in Drosophila embryos. *Science signaling*. 2:ra16.

Quintin, S., C. Gally, and M. Labouesse. 2008. Epithelial morphogenesis in embryos: asymmetries, motors and brakes. *Trends Genet*. 24:221-30.

Rauzi, M., P. Verant, T. Lecuit, and P.F. Lenne. 2008. Nature and anisotropy of cortical forces orienting Drosophila tissue morphogenesis. *Nat Cell Biol*. 10:1401-10.

Rodriguez-Diaz, A., Y. Toyama, D.L. Abravanel, J.M. Wiemann, A.R. Wells, U.S. Tulu, G.S. Edwards, and D.P. Kiehart. 2008. Actomyosin purse strings: renewable resources that make morphogenesis robust and resilient. *HFSP J*. 2:220-37.

Rolo, A., P. Skoglund, and R. Keller. 2009. Morphogenetic movements driving neural tube closure in Xenopus require myosin IIB. *Dev Biol*. 327:327-338.

Royou, A. 2002. Cortical recruitment of nonmuscle myosin II in early syncytial Drosophila embryos: its role in nuclear axial expansion and its regulation by Cdc2 activity. *The Journal of Cell Biology*. 158:127-137.

Sawyer, J.K., N.J. Harris, K.C. Slep, U. Gaul, and M. Peifer. 2009. The Drosophila afadin homologue Canoe regulates linkage of the actin cytoskeleton to adherens junctions during apical constriction. *J Cell Biol*. 186:57-73.

Shih, J., and R. Keller. 1992. Cell motility driving mediolateral intercalation in explants of Xenopus laevis. *Development*. 116:901-14.

Skoglund, P., A. Rolo, X. Chen, B. Gumbiner, and R. Keller. 2008. Convergence and extension at gastrulation require a myosin IIB-dependent cortical actin network. *Development*. 135:2435-2444.

Sokac, A.M., and E. Wieschaus. 2008. Zygotically controlled F-actin establishes cortical compartments to stabilize furrows during Drosophila cellularization. *Journal of Cell Science*. 121:1815-24.

Solon, J., A. Kaya-Copur, J. Colombelli, and D. Brunner. 2009. Pulsed forces timed by a ratchet-like mechanism drive directed tissue movement during dorsal closure. *Cell*. 137:1331-42.

Sweeton, D., S. Parks, M. Costa, and E. Wieschaus. 1991. Gastrulation in Drosophila: the formation of the ventral furrow and posterior midgut invaginations. *Development*. 112:775-89.

Vaezi, A., C. Bauer, V. Vasioukhin, and E. Fuchs. 2002. Actin cable dynamics and Rho/Rock orchestrate a polarized cytoskeletal architecture in the early steps of assembling a stratified epithelium. *Dev Cell*. 3:367-81.

Yonemura, S., M. Itoh, A. Nagafuchi, and S. Tsukita. 1995. Cell-to-cell adherens junction formation and actin filament organization: similarities and differences between non-polarized fibroblasts and polarized epithelial cells. *Journal of Cell Science*. 108 (Pt 1):127-42.

Figure Legends

Figure 1. Polarized apical constriction possibly reflects tissue mechanics. (A) Images of ventral furrow cell outlines in a live embryo using Spider-GFP. Scale bar = 10 μm. (B) Schematic showing the method used to calculate the aspect ratio (a/b) and anisotropy (x/y) of a cell. (C) Mean cross-sectional area (red) and anisotropy (blue) over time for a single embryo. Error bars are s.d. (n = 42 cells). (D) Box and whisker plot of aspect ratios from Spider-GFP, Resille-GFP, and *bicoid nanos torso-like(bnt)* Resille-GFP embryos. Boxes extend from 25th to 75th percentile with a line at the median. Whiskers extend to the most extreme values. Each sample represents 3 embryos, with 123, 102, and 158 cells. (E, F) Apical area and anisotropy (E) or constriction rate and the time derivative of anisotropy (F) for an individual cell over time. Anisotropy increases both during (i) and between (ii) contraction pulses.

Figure 2. AJs integrate global epithelial tension. (A) Myosin II in live wild-type or *arm*$^{M/Z}$ embryos. Myosin II initially starts to form a meshwork in *arm*$^{M/Z}$ (arrowheads), but the meshwork separates at discrete positions along the a-p axis. Scale bar = 10 μm. (B) Kymograph of actomyosin meshwork separation in *arm*$^{M/Z}$ embryo. Scale bar = 10 μm. (C) Tearing of the supracellular meshwork alters myosin II organization and dynamics. Myosin II fibers that normally extend between myosin II spots retract (blue arrows) in *arm*$^{M/Z}$ embryos (i). Loss of cell adhesion in *armRNAi* embryos causes myosin II to form rings (red and blue arrows) that contract (ii). Contracted myosin II rings in *armRNAi* embryos exhibit continuous, unrestrained cortical flow of myosin II spots (colored arrows) into the ring (iii). Scale bar = 5 μm.

Figure 3. Epithelial tension is highest along the length of the furrow. (A) Myosin-GFP images immediately after laser incisions (red lines, 20 μm) were made perpendicular to (top) or parallel to (bottom) the furrow. Myosin displacements perpendicular to these incisions (D_{ap} and D_{vl}) were measured. Scale bar = 20 μm. (B) D_{ap} and D_{vl} as a function of distance from the laser incision. The data was grouped into 4 μm bins (0-4, 4-8, etc . . .) and data points are mean ± s.e.m. (n = 4 embryos). (C) D_{ap} as a function of distance for H_2O injected (control) and *twiRNAi* embryos. Data points are the same as in B (n = 5 embryos). (D) Myosin-GFP images before (top) and after (bottom) a point ablation (cross-hairs). In the bottom panel, the post-ablation image (red) overlays the pre-ablation image (blue) to illustrate myosin displacement. Scale bar = 20 μm. (E) Schematic illustrating the method used for quantifying radial myosin displacement (D_r) in the direction (θ) relative to the a-p and v-l axes. Radial displacement is the component of the measured displacement (D) along direction θ. (F) D_r as a function of θ. The data was grouped into bins of 30° and data points are mean ± s.e.m. (n=5 embryos).

Figure 4. Anisotropic apical constriction results from a-p epithelial tension. (A and B) Apical myosin II (green) and subapical F-actin used to visualize cell outlines (white) in fixed *armRNAi* embryos. (A) shows a tear similar to those observed in live embryos. Red arrows indicate cells that have constricted isotropically. (B) is a later-staged embryo where myosin II has rounded up into rings. Scale bar = 10 μm. (C) Disruption of AJs results in loss of cell-cell adhesion. Time-lapse images of cell outlines (Spider-GFP) during a tear in an *armRNAi* embryo. Red cell-cell contacts are lost and different cells come into contact (blue). Scale bar = 5 μm. (D) Isotropic apical constriction occurs upon tearing. Time-lapse images of cell outlines (Spider-GFP) in an *E-CadherinRNAi* embryo. Blue dots indicate initially anisotropic cells that constrict isotropically

upon loss of epithelial integrity. Scale bar = 5 μm. Apical area (E) and anisotropy (F) were quantified for the cells labeled in D. Dotted line indicates the time of the tear.

Figure 5. Spot AJs integrate actomyosin fibers to form a supracellular meshwork. (A) Apical myosin II (green) and subapical E-cadherin, ~ 2 μm below the apical cortex (purple), in fixed embryos. Schematics indicating the stage of furrow formation are shown above each image pair. Scale bar = 5 μm. (B) Magnified view of supracellular actomyosin fibers. Apical myosin II (green), subapical E-cadherin (purple), and apical actin filaments (cyan) were imaged in fixed embryos. Supracellular actomyosin fibers are often oriented perpendicular to cell interfaces (i, arrows), but can also be seen running parallel to cell interfaces (ii, arrows). Actomyosin fibers often radiated from a central myosin II spot or ring (red asterisks). Bottom-middle images were thresholded to facilitate visualization of myosin II fibers. Scale bar = 5 μm. (C) Apical E-cadherin (purple) and myosin II (green) in fixed embryos. Subapical E-cadherin staining is used to illustrate cell outlines. Myosin II fibers connect to apical E-cadherin punctae, or spot AJs (arrows). In late stages, spot AJs can appear stretched along the fiber (yellow asterisks). Scale bar = 5 μm.

Figure 6. Sensitizing AJs disrupts intracellular connections between the actomyosin cytoskeleton and the plasma membrane. (A) SEM of ventral furrows in wild-type embryos. Scale bars = 5 μm. (B, C) SEM of $arm^{M/Z}$ embryos. Membrane tethers extend between dissociated cells (B) and across epithelial tears (C). Scale bars = 5 μm. (D) Myosin II localizes to regions of membrane blebs that are interconnected by membrane tethers. Images of apical myosin II (red, Myosin-mCherry), apical membrane (green, Spider-GFP), and subapical

membrane (purple) in live *armRNAi* embryos. Scale bar = 10 μm. (E) Model: Lower adhesion in *arm* mutants causes higher tension per adhesive structure, leading to the rupture of fiber-AJ connections.

Figure 7. Snail and Twist are required for epithelial tearing. (A) Images of Myosin-GFP in live embryos injected with the indicated dsRNA. *snaRNAi* inhibits the formation of myosin II rings and the loss of cell-cell adhesion normally observed in *armRNAi* embryos. *twiRNAi* inhibits tearing, but myosin contractions still occur. Scale bar = 10 μm. (B) Images of cell outlines (Spider-GFP) in *armRNAi* and *arm-twiRNAi* embryos. Knock-down of Twist suppresses the formation of discrete epithelial tears. Scale bar = 10 μm. (C) Epithelial tears and loss of cell-cell adhesion occur within the Snail expression domain. Images of a fixed $arm^{M/Z}$ embryo stained for Snail (green) and Neurotactin (purple, cell outlines). An apical image of Neurotactin is included to illustrate the position of the tear. The ventral midline is offset to visualize the lateral border of the mesoderm where two Snail-expressing nuclei do not initially lose adhesion (white bracket). Scale bar = 10 μm.

Figure 8. Twist is required for myosin II stabilization and supracellular meshwork formation. (A) Twist is required to stabilize apical myosin II fibers after contraction. Time-lapse images of Myosin-GFP (green) and Membrane-mCherry (purple). Scale bar = 5 μm. (B) Quantification of apical area (red) and myosin intensity (blue) in individual cells from wild-type and *twiRNAi* embryos. (C) Twist is required to maintain cortical myosin II after a contraction pulse. Normalized myosin intensity for individual contraction pulses were averaged. Data are means ± s. d. (control, n = 329 pulses, 120 cells, 2 embryos; *twiRNAi*, n = 524 pulses, 106 cells, 2

embryos). (D) Twist is required to stabilize myosin II rings. Time-lapse images of Myosin-GFP in embryos treated with *arm* dsRNA together with either *twi* or *fog/t48* dsRNA. Scale bar = 5 μm. (E) Myosin-GFP (top and bottom, green) in live control or *twiRNAi* embryos. Images were segmented using intensity and area thresholds to identify myosin II structures (bottom, red). Scale bar = 10 μm. (F) Twist is required to form the supracellular actomyosin meshwork. The area of the largest myosin II structure was quantified for each time point in videos of control injected or *twiRNAi* embryos.

Figure 9. Causes and consequences of contractile force integration. (A) Distribution of apical tensile forces that accompany ventral furrow formation. Black arrows indicate the movement of lateral cells towards the ventral midline. Red arrows indicate epithelial tension, which is predominantly directed along the length of the furrow (a-p axis). (B) Tissue-level forces influence individual cell shape changes. Ventral furrow cells attempt to constrict isotropically (black arrows), but a-p tension (red arrows) resists constriction in this direction, resulting in anisotropic constriction. (C) Model for how contractile forces are integrated to generate epithelial tension in the ventral furrow. In wild-type embryos, pulses of actin (red) and myosin II (green) contraction constrict cell apices and actomyosin fibers that remain on the apical surface between pulses maintain cortical tension (black arrows above cells), thus stabilizing cell shape. Actomyosin fibers linked by spot AJs (blue) form a supracellular meshwork that allows forces to be stably transmitted between cells, generating global epithelial tension (red arrows). In the absence of Twist, cells lack actomyosin fibers between contractions and fail to assemble a supracellular actomyosin meshwork. Thus, contraction pulses in cells stretch their immediate neighbors and tension fails to be propagated across the epithelium.

Supplemental Figure Legends

Supplemental Figure 1. Knock-down of E-cadherin or α-catenin disrupts the myosin II network and results in membrane tethers. (A) RT-PCR of *ECad2*, *arm*, and *α-catenin* transcripts after RNAi. The percent knock-down of the specific transcript was measured to be 60% for *ECad2RNAi* and 90-95% for *armRNAi* and *α-cateninRNAi*. (B) Myosin-GFP in live *ECad2RNAi* and *α-cateninRNAi* embryos. Bottom images are 5 minutes later than top images. Note the dramatic tears along the a-p axis and the contraction of myosin II into rings. Scale bar = 10 μm. (C) Myosin II rings in *armRNAi* embryos are enriched in the remaining cortical E-cadherin. Images represent fixed Myosin-GFP *armRNAi* embryos stained for E-cadherin. Scale bar = 5 μm. (D) Membrane tethers contain F-actin, but not myosin II. Fixed Myosin-GFP (top) or Membrane-GFP (Spider-GFP, bottom) *armRNAi* embryos were stained for F-actin. Arrowheads indicate membrane tethers that appear to contain F-actin. Scale bar = 5 μm. (E) Apical membrane (Spider-GFP) in live *ECad2RNAi* and *α-cateninRNAi* embryos. Membrane tethers connect dense membrane accumulations, similar to *armRNAi* embryos. Scale bar = 5 μm. (F) Scanning electron microscopy (SEM) of *armRNAi* and *arm-twiRNAi* embryos. In *arm-twiRNAi* embryos, cells dissociate and continue to form numerous blebs and tethers. Scale bar = 5 μm.

Supplemental Figure 2. Myosin-GFP displacement as a function of time for different laser ablation experiments. Individual curves represent the displacement of individual myosin II structures that retracted various distances after laser ablation. Gray box indicates the duration of the ablation. Arrows indicate the time when displacements were measured for the data in Figure 3. Line ablations (left panel) lasted ~ 6.4 seconds and thus the tissue relaxed farther before the first post-ablation image. Point ablations (right panel) lasted 0.67 seconds, providing a better estimate for the initial retraction velocity.

Supplemental Video Legends

Video 1. Maximum intensity Z-projections of Myosin-GFP during ventral furrow formation in wild-type and $arm^{M/Z}$ mutant embryos. Images were analyzed by time-lapse confocal microscopy using a laser-scanning confocal microscope (Leica SP5). Image stacks were taken every 12 sec. Video is sped up 120-fold faster than real-time (10 frames/second). Related still images in Figure 2A.

Video 2. Maximum intensity Z-projections of Myosin-GFP in embryos where a laser incision was made in the myosin II meshwork. The white bars in the first frame illustrate the location of the incision made in each embryo. Images were analyzed by time-lapse confocal microscopy using a spinning-disk confocal microscope (PerkinElmer Ultraview). Image stacks were taken every 3 sec. Video is sped up 30-fold faster than real-time (10 frames/second). Related still images in Figure 3A.

Video 3. Maximum intensity Z-projection of Myosin-mCherry (top) and single Z-slice of Membrane-GFP below the apical surface (bottom, to illustrate cell outlines) in an *armRNAi* embryo. Images were analyzed by time-lapse confocal microscopy using a laser-scanning confocal microscope (Leica SP5). Image stacks were taken every 19.5 sec. Video is sped up 120-fold faster than real-time (6.15 frames/second).

Video 4. Maximum intensity Z-projection of Myosin-GFP in an $arm^{M/Z}$ mutant embryo. Myosin fiber contracts upon separation of the actomyosin meshwork. Images were analyzed by time-lapse confocal microscopy using a spinning-disk confocal microscope (PerkinElmer Ultraview). Image stacks were taken every 2.4 sec. Video is sped up 10-fold faster than real-time (4.18 frames/second). Related still images in Figure 2C, i.

Video 5. Maximum intensity Z-projection of Myosin-GFP in an *armRNAi* embryo. Tears in the meshwork are associated with myosin contraction into rings or balls and constitutive flow of myosin spots into these rings. Images were analyzed by time-lapse confocal microscopy using a spinning-disk confocal microscope (PerkinElmer Ultraview). Image stacks were taken every 2.4 sec. Video is sped up 30-fold faster than real-time (12.66 frames/second). Related still images in Figure 2C, iii.

Video 6. Membrane tether formation in a Membrane-GFP (Spider) embryo. Time-lapse images were taken of a single Z-slice on the apical surface of an *armRNAi* embryo. Images were analyzed by time-lapse confocal microscopy using a laser-scanning confocal microscope (Leica SP5). Image stacks were taken every 6 sec. Video is sped up 120-fold faster than real time (20 frames/second).

Video 7. Maximum intensity Z-projection of Myosin-GFP in an *arm-CG3651RNAi* embryo. Images were analyzed by time-lapse confocal microscopy using a spinning-disk confocal microscope (PerkinElmer Ultraview). Image stacks were taken every 2.75 sec. Video is sped up 60-fold faster than real-time (21.82 frames/second). Related still image in Figure 7A.

Video 8. Maximum intensity Z-projection of Myosin-GFP in *arm-snaRNAi* embryo. *snaRNAi* inhibits loss of cell adhesion and epithelial tears. Cells only round up when they eventually enter mitosis. Images were analyzed by time-lapse confocal microscopy using a spinning-disk confocal microscope (PerkinElmer Ultraview). Image stacks were taken every 2.34 sec. Video is sped up 60-fold faster than real-time (25.64 frames/second). Related still image in Figure 7A.

Video 9. Maximum intensity Z-projection of Myosin-GFP in *arm-twiRNAi* embryo. *twiRNAi* does not prevent loss of adhesion, but inhibits the formation of discrete epithelial tears. Note that contraction pulses occur even when cells appear to lose adhesion. Images were analyzed by time-lapse confocal microscopy using a spinning-disk confocal microscope (PerkinElmer Ultraview). Image stacks were taken every 2.75 sec. Video is sped up 60-fold faster than real-time (21.82 frames/second). Related still image in Figure 7A.

Video 10. Single Z-slice of Membrane-GFP (Spider) in *arm-twiRNAi* embryo. Note that *twiRNAi* inhibits the formation of discrete tears as cells lose adhesion. Images were analyzed by time-lapse confocal microscopy using a laser-scanning confocal microscope (Leica SP5). Image stacks were taken every 11 sec. Video is sped up 60-fold faster than real-time (5.5 frames/second). Related still image in Figure 7B.

Figure 1

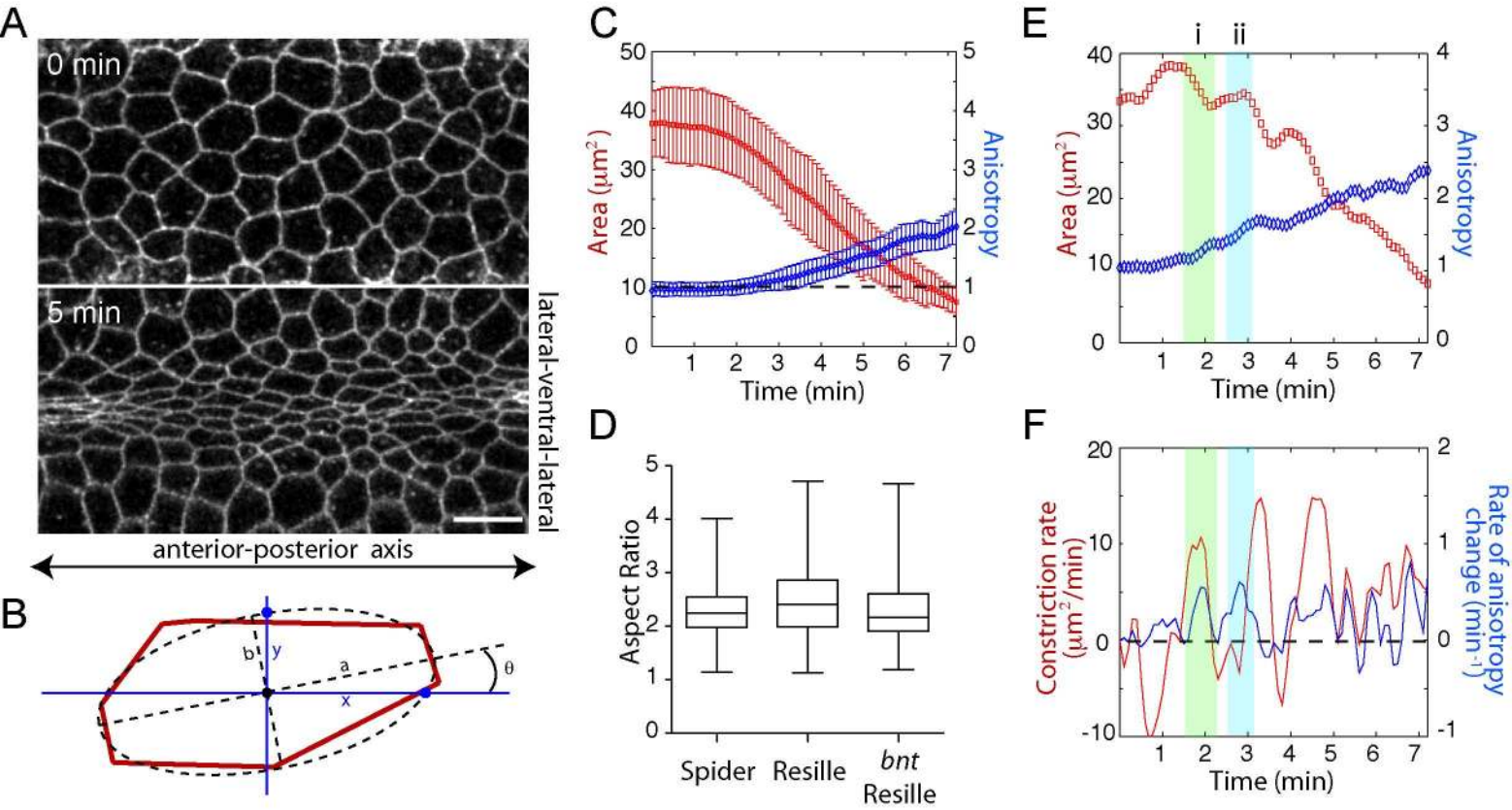
A
0 min
5 min
lateral-ventral-lateral
anterior-posterior axis
B
b
y
a
x
θ
C
Area (μm²)
Anisotropy
Time (min)
D
Aspect Ratio
Spider
Resille
bnt Resille
E
i
ii
Area (μm²)
Anisotropy
Time (min)
F
Constriction rate (μm²/min)
Rate of anisotropy change (min⁻¹)
Time (min)

Figure 2

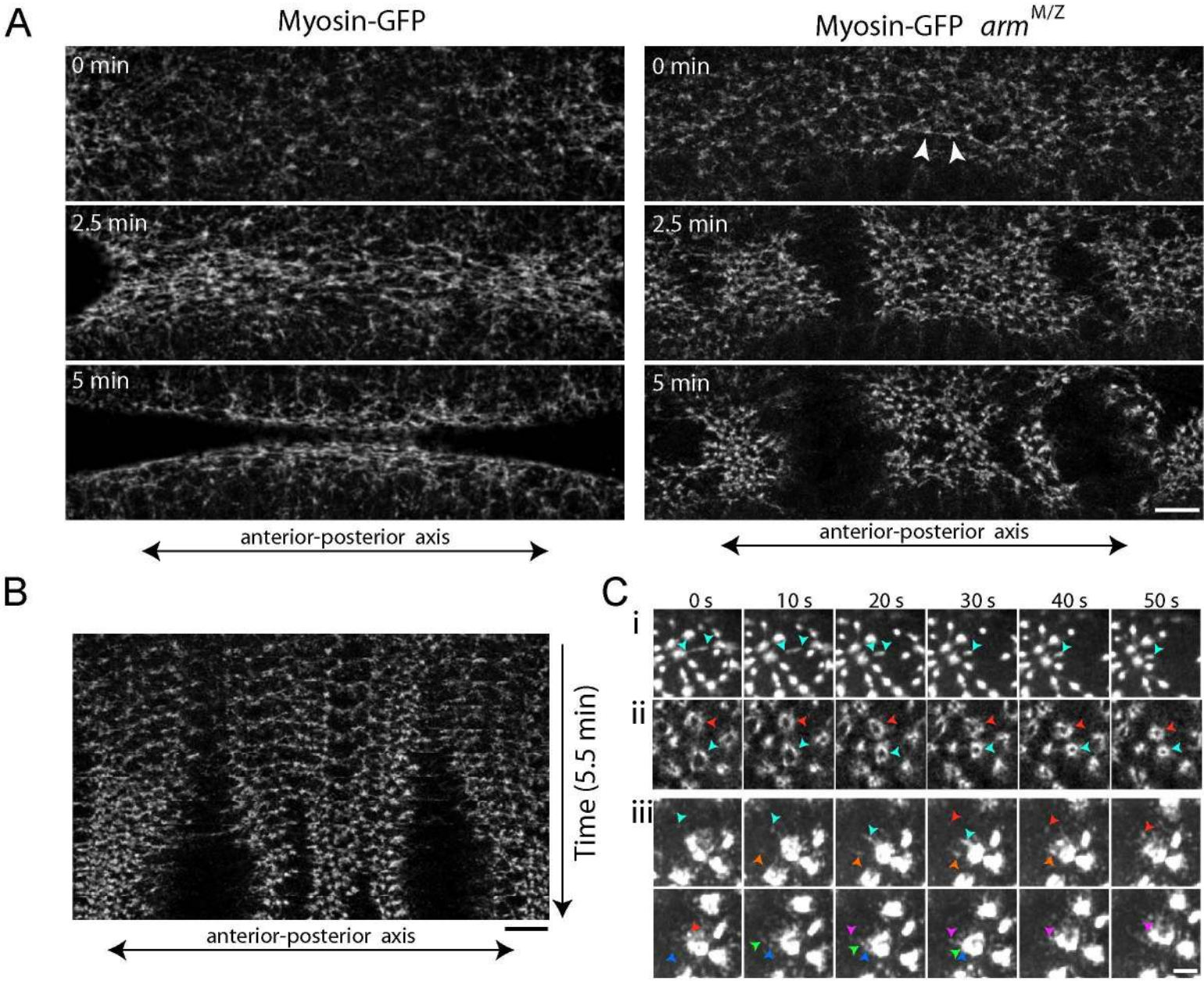
A
Myosin-GFP
Myosin-GFP arm M/Z
0 min
2.5 min
5 min
0 min
2.5 min
5 min
anterior-posterior axis
anterior-posterior axis
B
Time (5.5 min)
anterior-posterior axis
C
0 s
10 s
20 s
30 s
40 s
50 s
i
ii
iii

Figure 3

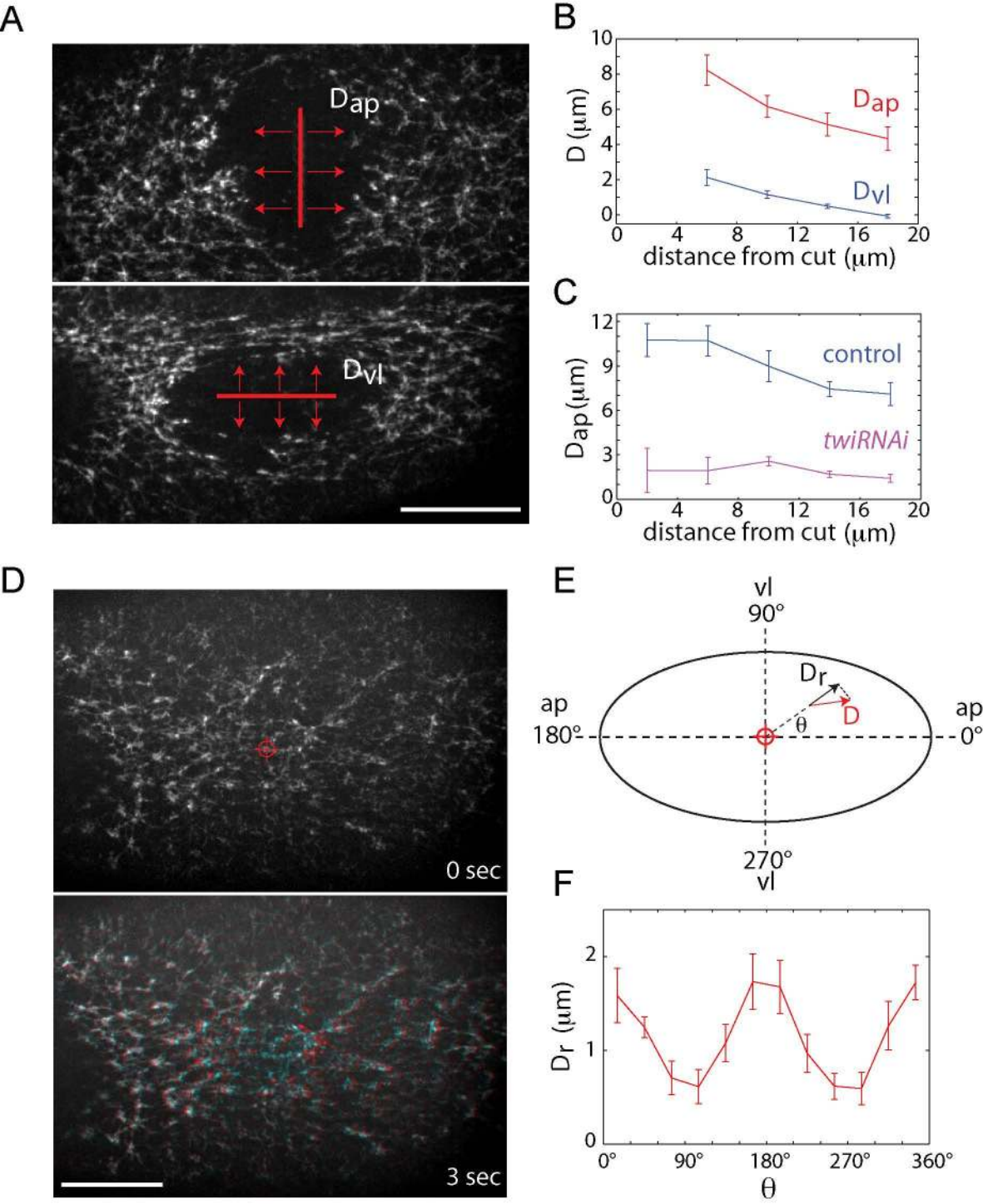
A
Dap
Dvl
B
D (μm)
Dap
Dvl
distance from cut (μm)
C
Dap (μm)
control
twiRNAi
distance from cut (μm)
D
0 sec
3 sec
E
vl
90°
ap
180°
ap
0°
270°
vl
Dr
D
θ
F
Dr (μm)
θ

Figure 4

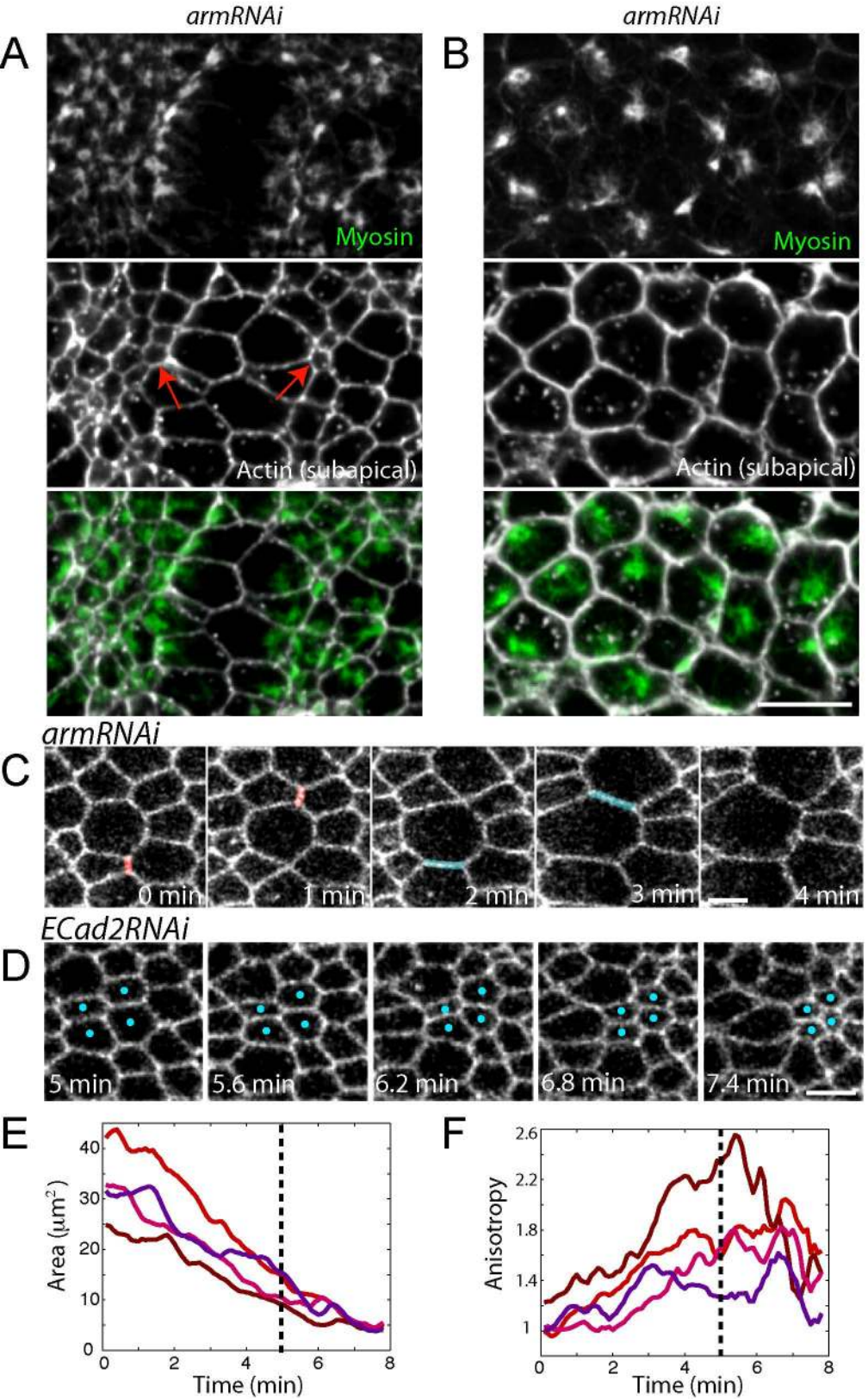
armRNAi
armRNAi
A
B
Myosin
Myosin
Actin (subapical)
Actin (subapical)
armRNAi
C
0 min
1 min
2 min
3 min
4 min
ECad2RNAi
D
5 min
5.6 min
6.2 min
6.8 min
7.4 min
E
Area (μm²)
Time (min)
F
Anisotropy
Time (min)

Figure 5

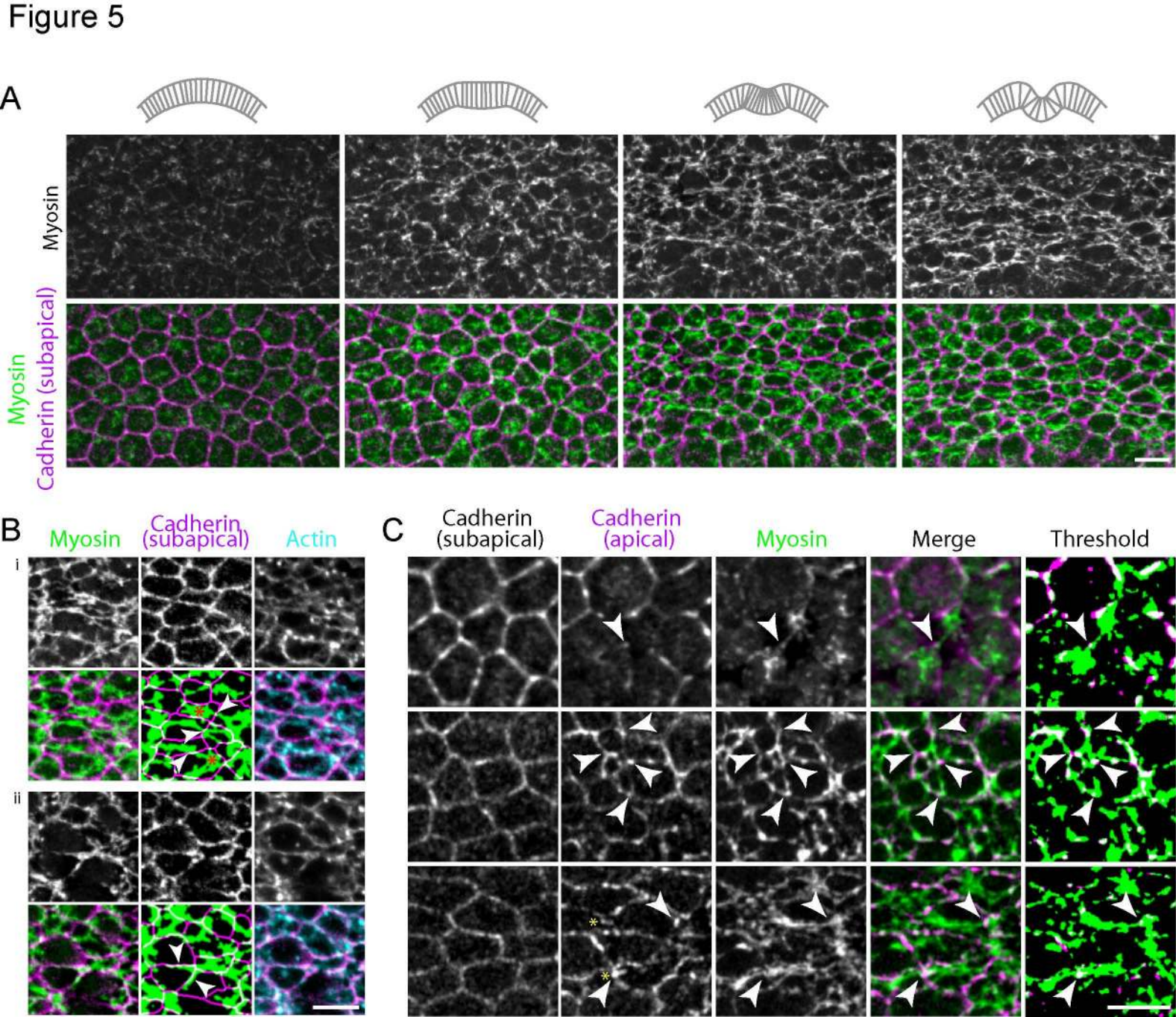
A
Myosin
Myosin
Cadherin (subapical)
B
Myosin
Cadherin (subapical)
Actin
i
ii
C
Cadherin (subapical)
Cadherin (apical)
Myosin
Merge
Threshold

Figure 6

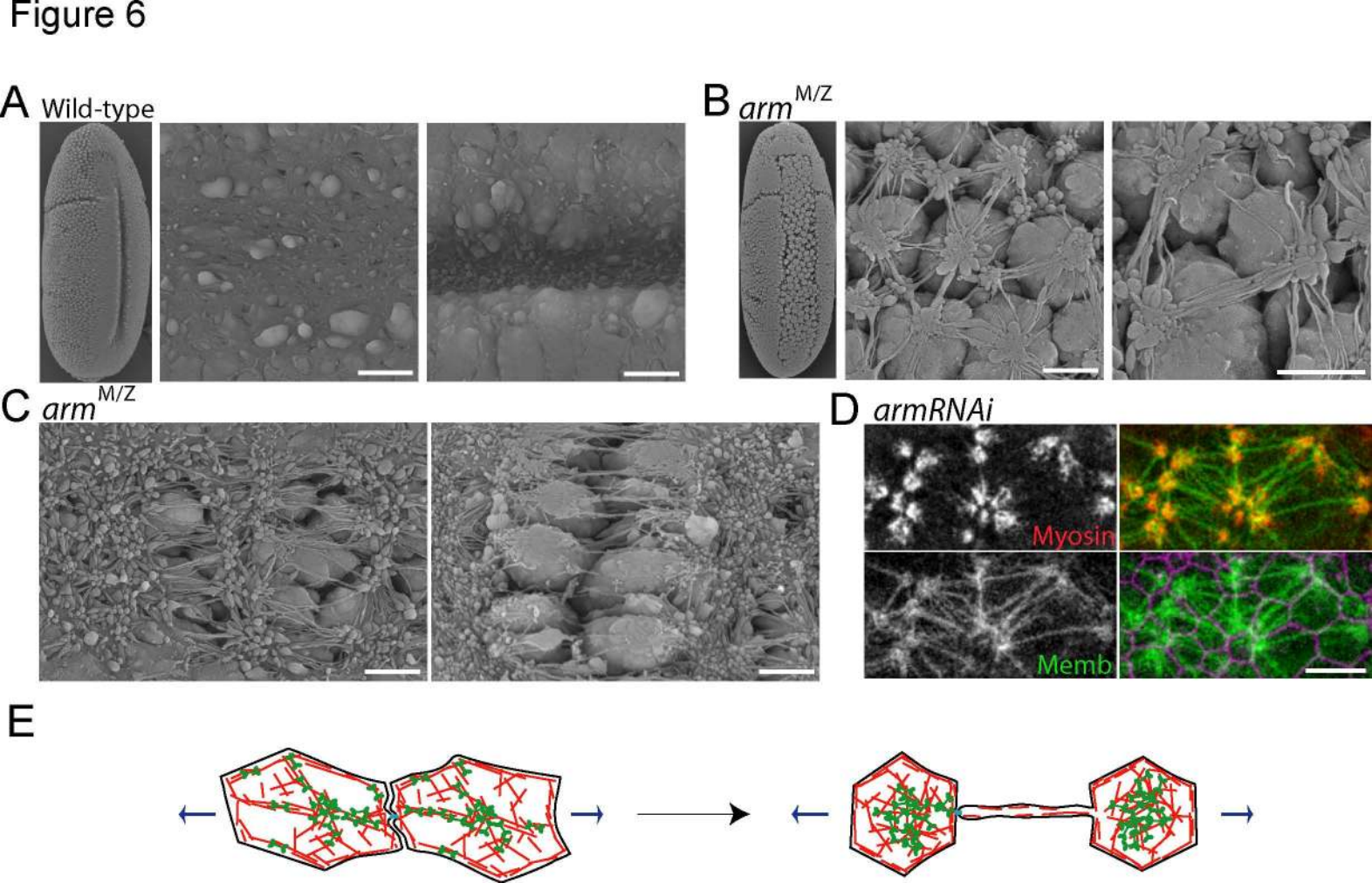

Figure 7

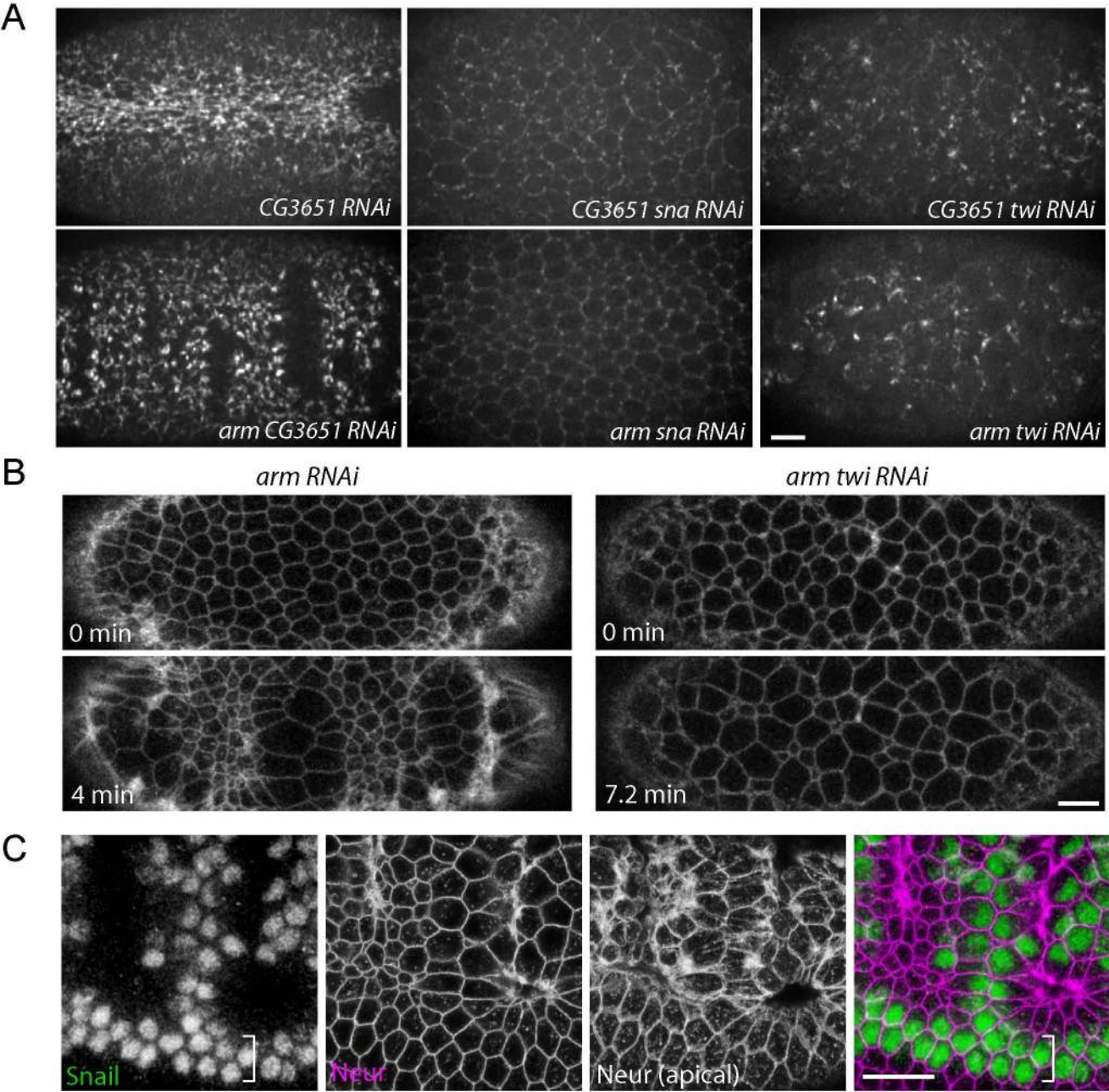
A
CG3651 RNAi
CG3651 sna RNAi
CG3651 twi RNAi
arm CG3651 RNAi
arm sna RNAi
arm twi RNAi
B
arm RNAi
arm twi RNAi
0 min
0 min
4 min
7.2 min
C
Snail
Neur
Neur (apical)

Figure 8

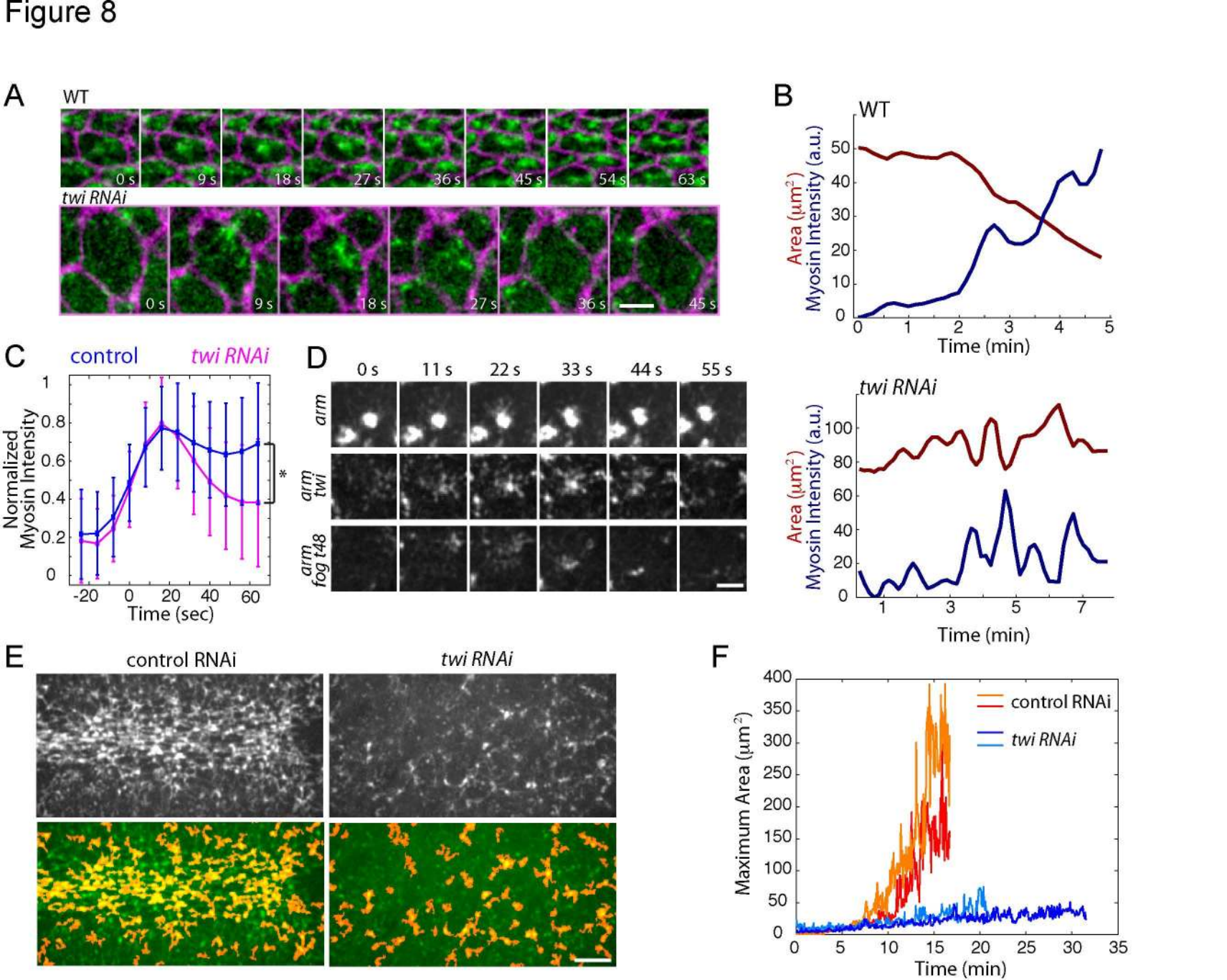
A
WT
0 s
9 s
18 s
27 s
36 s
45 s
54 s
63 s
twi RNAi
0 s
9 s
18 s
27 s
36 s
45 s
B
WT
Area (μm²)
Myosin Intensity (a.u.)
Time (min)
twi RNAi
Area (μm²)
Myosin Intensity (a.u.)
Time (min)
C
control
twi RNAi
Normalized Myosin Intensity
Time (sec)
*
D
0 s
11 s
22 s
33 s
44 s
55 s
arm
arm twi
arm fog t48
E
control RNAi
twi RNAi
F
control RNAi
twi RNAi
Maximum Area (μm²)
Time (min)

Figure 9